JOURNAL OF AIRCRAFT
Vol. 32, No. 1, January–February 1995

Simulation and Model Reduction for the Active Flexible Wing Program

Carey Buttrill,* Barton Bacon,† Jennifer Heeg,‡ and Jacob Houck§
NASA Langley Research Center, Hampton, Virginia 23681
and
David Wood¶
Unisys Government Systems, Inc., Hampton, Virginia 23666

The simulation methodology used in the Active Flexible Wing wind-tunnel test program is described. An overview of the aeroservoelastic modeling used in building the required batch and hot-bench simulations is presented. Successful hot-bench implementation required that the full mathematical model be significantly reduced while assuring that accuracy be maintained for all combinations of 10 inputs and 56 outputs. The reduction was accomplished by using a method based on internally balanced realizations and by focusing on the linear, aeroelastic portion of the full mathematical model. The error-bound properties of the internally balanced realization significantly contribute to its utility in the model reduction process. The reduction method and the results achieved are described.

Introduction

MINIMIZING weight is vital to any successful aircraft design. An aircraft must be flutter-free at some percentage (the safety margin) beyond its operating envelope. Flutter is a dynamic instability that occurs on aircraft at a dynamic pressure and Mach condition wherein the structure begins to extract energy from the fluid flow. Traditional, passive remedies for flutter problems add weight in the form of additional structure or mass ballast. If the flutter-free requirement for an aircraft design can be met by active stabilization using existing control surfaces, significant weight savings may be possible.

Wind-tunnel tests of active flutter suppression control systems were conducted in the Transonic Dynamics Tunnel (TDT) at the Langley Research Center (LaRC). The test model was a full-span, free-to-roll, aeroelastically-scaled model of an advanced fighter and is referred to in this article as the Active Flexible Wing (AFW) wind-tunnel model. The AFW wind-tunnel model has been utilized in two research programs[1,2] involving four tunnel entries: 1986, 1987, 1989, and 1991. The demonstration of active flutter suppression was a program objective for the last two entries. The objective of the 1989 test was to evaluate flutter suppression and rolling maneuver load control systems as individual functions. The objective of the 1991 test was to demonstrate active flutter suppression while simultaneously performing aggressive rolling maneuvers in which wing loads were controlled.

The flutter mechanism of the AFW model was of the clean-wing, classical variety with a rapid onset. Failure of the active flutter suppression system while testing above open-loop flutter conditions would put both the model and the tunnel at risk. An extensive simulation-based testing and validation effort was needed for the AFW program flutter suppression investigations. Simulations produced to support the 1989 and 1991 tunnel entries are the subject of Refs. 3, 4, and this article.

Both batch and hot-bench simulations were developed for each tunnel entry. The batch simulations served as "truth" models and were used to 1) evaluate the control laws by predicting performance and establishing margins, 2) provide data files for the hot-bench simulations, and 3) verify the hot-bench simulations. The hot-bench simulations of the model in the wind-tunnel environment served to support validation and testing of the digital controller system.

The simulation mathematical model developed for the 1991 tunnel test was too large[4] to provide an effective hot-bench simulation. Substantial math model reduction was required without compromising response accuracy. The model reduction methodology applied to the 1991 mathematical model was based on the well known properties of the internally balanced (IB) realization of a linear time-invariant system.[5,6] When an asymptotically stable system is transformed into IB coordinates, the resulting states are ordered in their importance to the system's output/input response.[5] An easily calculated bound exists for determining the error introduced by truncating the least significant IB states.[5,6] Furthermore, this bound applies to the maximum frequency response error over all frequencies for all possible input-output paths. The IB method was extended by Enns,[7] who developed an approach based on frequency-weighted internally balanced coordinates, whereby frequency regions could be selected for emphasis by the use of weighting filters. Bacon[8] extended the frequency-weighted internally balanced approach, producing a frequency-weighted pole-preserving method to better accommodate a system with unstable or neutrally stable components. For the work described herein, the classical IB method of handling unstable subsystems by decoupling the stable and unstable portions was applied without frequency weighting. When the IB method was combined with appropriate scaling and a reasonable error bound, a reduction method emerged that could be applied to a collection of linear models with high confidence and little adjustment. The success encountered in applying an IB approach to aeroelastic systems of realistic size and complexity is significant in that it offers an

Received May 13, 1992; revision received March 7, 1994; accepted for publication March 21, 1994.

*Research Engineer, Dynamics and Control Branch. Senior Member AIAA.
†Aerospace Research Engineer, Dynamics and Control Branch.
‡Research Engineer, Aeroelasticity Branch. Member AIAA.
§Group Lead, Flight Simulation Applications. Associate Fellow AIAA.
¶Simulation Programmer/Analyst.

additional approach to the research that has been performed in minimizing the impact of unsteady aerodynamic states on the size of aeroelastic systems.[9,10]

Wind-Tunnel Model

The AFW wind-tunnel model could be tested either fixed in roll or free to roll about the sting axis. As seen in Fig. 1 of the AFW summary article by Perry et al., in this issue, the wind-tunnel model had 8 control surfaces which could be commanded and 40 primary sensor outputs. The primary outputs included 8 control surface position measurements, 13 accelerometer outputs, 8 strain gauge outputs, 8 hinge moment measurements, and model pitch position, roll position, and roll rate.

To support flutter suppression investigations, a destabilizing mass ballast was added to each wingtip so that the model would flutter within the operating envelope of the TDT.[2] The tip ballast served to lower both the first-bending and the first-torsion elastic mode frequencies with the predominant effect on the first-torsion mode. The result was that the first-torsion and the first-bending elastic modes combined to form the primary flutter mechanism at a lower dynamic pressure than was the case for the original wind-tunnel model (with no tip ballast). The tip ballast could also be rapidly decoupled in pitch from the wingtip by releasing a hydraulic brake. Ideally, when decoupled, the tip ballast was sufficiently free to rotate about the pivot mechanism so that as the wing participates in its torsional modes, the tip ballast would remain level. In actual practice, the tip ballast was restrained in pitch by a soft spring that was tuned to be stiff enough that the tip ballast would not depart in pitch due to static airloads, yet soft enough that the decoupled boundary was well beyond the tunnel operating range. Decoupling the tip ballast proved to be an effective flutter stopper during testing, providing additional safety margin. The AFW wind-tunnel model is described in greater detail in Refs. 1 and 2.

Hot-Bench Simulation Setup

The AFW hot-bench simulation setup utilized the central real-time facility at LaRC. The LaRC real-time facility consists of nodes that communicate by means of a fiber-optic digital-data network. For the AFW hot-bench simulation, one of LaRC's two production real-time computers was used to integrate the equations of motion. A graphics computer provided a real-time display. The display presented model roll, control surface deflections, and total structural deformation of the simulated wind-tunnel model. Communications with the digital controller occurred over analog lines in the same manner as occurred when the controller was connected to the physical model at the wind tunnel.

During both hot-bench simulation and tunnel testing, signals to and from the digital controller went through interface electronics. The interface contained trip logic that tested for a variety of exceedances. In addition, the interface electronics housed anti-aliasing filters that condition the signals from the wind-tunnel model before being sampled by the digital controller.

While in the hot-bench laboratory the analog anti-aliasing filters in the model/controller interface electronics were bypassed. The antialiasing filter dynamics were included in the simulation of the wind-tunnel model. The hot-bench environment was relatively noise-free when compared to the wind-tunnel environment, and the absence of anti-aliasing filters in the hot-bench setup was not a difficulty. The presence of analog dynamic elements would have interfered with the need, discussed in a subsequent section, to run at a variety of time scales. Real-time simulations supported at the LaRC facility are typically run without anti-aliasing filters unless problems are noted.

Simulation Mathematical Models

An overview of the structure of the batch and hot-bench simulations and the data flow between them is shown in Fig. 1. As indicated in Fig. 1, there are 10 inputs (8 actuator commands and 2 Gaussian random number turbulence inputs) into the simulation continuous system mathematical model. Fifty-six outputs are generated. The first 40 outputs represent the simulated wind-tunnel model sensor outputs. The last 16 outputs are the displacements of the generalized coordinates associated with 16 (2 × first 8 per symmetry) elastic modes and are required to drive the graphics display. The method of discretization used in the hot-bench simulation and the method whereby the hot-bench simulation is generated automatically from the batch simulation are described in Ref. 3.

Actuator Models

Frequency responses for the eight individual actuators were measured with the wing elastic motion restrained. Third-order transfer functions, with parameters optimized in a least-square sense, produced good fits (in the frequency range of interest) to measured frequency response data. In general, right and left members of an actuator pair required different parameters to achieve a good fit, and were therefore modeled individually. The third-order transfer function models allowed position, velocity, and acceleration of individual control surfaces to be predicted. The outputs of the right and left actuator models were resolved into symmetric and antisymmetric components that became inputs into the aeroelastic equations.

All the actuator position/command transfer functions had the following form:

$$\frac{\delta(s)}{\delta_c(s)} = \frac{k_\delta a_\delta \omega_\delta^2}{(s + a_\delta)(s^2 + 2\zeta_\delta \omega_\delta s + \omega_\delta^2)} \tag{1}$$

where $\delta(s)$ is the control surface position, $\delta_c(s)$ is the command, k_δ is the steady-state gain, a_δ is the first-order pole location, ζ_δ is the damping of the complex pair, and ω_δ is the frequency of the complex pair. The first-order pole reflects the dynamics of hydraulic fluid flowing through a small orifice whose size is regulated by position feedback error. The second-order complex pair results from the compressibility of the hydraulic fluid together with compliance of the structure and the magnitude of the position error feedback gain. Rate limits, as a function of load, were specified by the manufacturer. The rate limit arises in a first-order approximation from the maximum rate that hydraulic fluid can pass through a small orifice for a given difference between supply and cham-

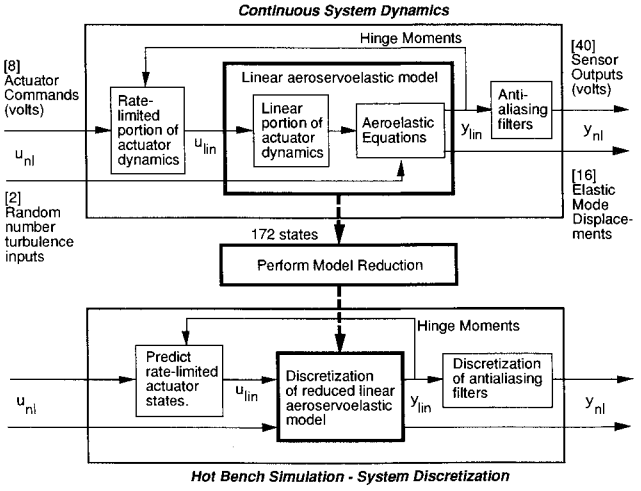

Fig. 1 Data flow from the batch to the hot-bench simulation.

ber pressures. Positive and negative rate limits based on no-load rate limits modified by hinge moment were formed

$$rl_{\text{pos}} = (rl_{\text{nl}})\sqrt{1 - (HM_\delta/HM_{\delta_{\text{STALL}}})} \quad (2)$$

$$rl_{\text{neg}} = (rl_{\text{nl}})\sqrt{1 + (HM_\delta/HM_{\delta_{\text{STALL}}})} \quad (3)$$

where the hinge moment HM_δ is positive for an external load resisting positive actuator motion, and $HM_{\delta_{\text{STALL}}}$ represents the maximum load the actuators can overcome. Note that an aiding load will produce a rate limit larger than the no-load rate limit rl_{nl}. An aiding load could occur when a leading-edge surface is driven away from the zero deflection condition and when a trailing-edge surface is driven toward a zero deflection.

Turbulence Model

A turbulence model based on the Dryden atmospheric turbulence model[11] was used. A break frequency of 17.23 Hz for the turbulence transfer function was used to approximate the expected wind-tunnel turbulence. Resonance peaks at 10 Hz were observed in tunnel data from prior entries, and the predicted flutter frequency was expected to be near 10 Hz. A break frequency of 17.23 Hz produces a peak magnitude at 10 Hz in the Dryden transfer function. The simulation transfer function equations used for each symmetry are

$$\frac{\xi_g(s)}{v(s)} = \sigma_g \sqrt{\frac{\tau_g}{T_v}} \frac{1 + \sqrt{3}(\tau_g s)}{(1 + \tau_g s)^2} \quad (4)$$

where $\xi_g(s)$ is the Laplace transform of the modal participation coefficient for the gust mode, $v(s)$ is the Laplace transform of the digital Gaussian random process that is sampled and held every T_v s, τ_g^{-1} is the break frequency in rad/s, and σ_g is the rms turbulence intensity. In both the batch and hot-bench simulations, T_v is the integration step size. The factor of $\sqrt{(1/T_v)}$ applied to the input $v(s)$ arises from the inherently band-limited nature of a digital simulation. A more complete description of the gust mode shapes used to model the turbulence can be found in Ref. 12.

When the wind-tunnel model is subjected to natural wind-tunnel turbulence with a flutter-suppression control law engaged, control surface activity results. Three different flutter control laws were tested in the November 1989 tunnel test, and all generally resulted in the same observed rms levels.[13] By making the turbulence intensities functions of dynamic pressure, simulation-predicted rms levels for control activity could be brought into agreement with observed data. An example of this process is shown in Fig. 2 for the flutter suppression control law that achieved the highest dynamic pressure in the 1989 test. The intensities required to bring batch-simulation-generated rms results for both commanded control positions and control rates into agreement with experimental data are plotted in Fig. 2 as functions of dynamic pressure. Beyond the dynamic pressure of 275 psf, there were no experimental data from the 1989 test. However, a simulation model was required that could be used up to 350 psf, and so extrapolation was performed. For each symmetry, one intensity function corrects the rms rate predictions, and the other corrects the rms deflection predictions. Since only one intensity exists per symmetry, either the rms rate results or the rms position results, but not both, can be matched. The intensity functions used in simulation prior to the 1991 entry are shown as solid lines (one per symmetry) on Fig. 2 and are given by the following functions:

$$\sigma_{g_{sy}} = 0.4 + 1.0(\bar{q}/100) \quad \text{and} \quad \sigma_{g_{as}} = 1.6 + 2.4(\bar{q}/100) \quad (5)$$

where $\bar{q}$ is dynamic pressure in units of psf. These estimates of intensity are highly configuration-dependent and should not be regarded as a final characterization of turbulence in the TDT.

Figure 3 shows the rms commanded control rates predicted prior to the 1991 test along with commanded control rates actually observed for the flutter suppression control law described in Ref. 14. Attempts to be conservative were generally successful. Intensities were chosen as a function of dynamic pressure that resembled an upper bound (Fig. 2). Beyond a dynamic pressure of 200 psf, control activity was overpredicted.

Structural Model

Two finite element structural representations of the AFW wind-tunnel model were available. These structural models had on the order of 3400 degrees of freedom (DOF), and represented the symmetric and the antisymmetric wind-tunnel model fixed in roll and with the tip store coupled. From these two finite element structural models, six sets of reduced-order structural influence coefficient matrices were generated by defining a set of load points on the model, generally in the z direction. These symmetric and antisymmetric structural influence coefficient matrices represent the wind-tunnel model fixed and free in roll with the tip store coupled and decoupled. Note that the symmetric influence coefficient matrices remain unchanged when the wind-tunnel model sting condition changes from fixed in roll to free in roll. For the 1991 math models, the number of load points was 204 for the symmetric models and 218 for the antisymmetric models. A column of the structural influence coefficient matrix was generated by imposing a unit force at one load point and recording the resulting deflections induced at all the load points. These structural influence coefficient matrices were combined with an appropriately dimensioned lumped mass matrix in an eigenvalue analysis to generate natural frequencies and mode shapes. The resulting eigenvectors (mode shapes) were scaled such

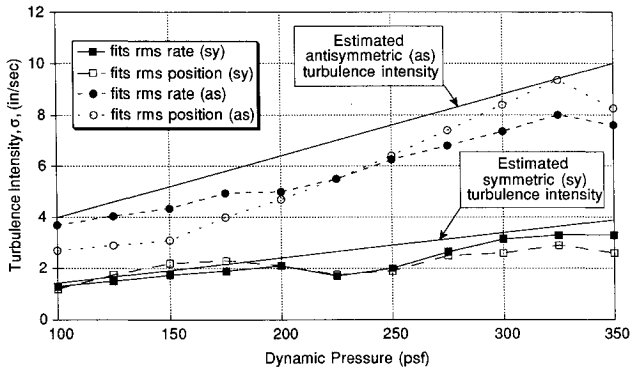

Fig. 2 Turbulence intensities used for 1991 simulation derived from 1989 test results.

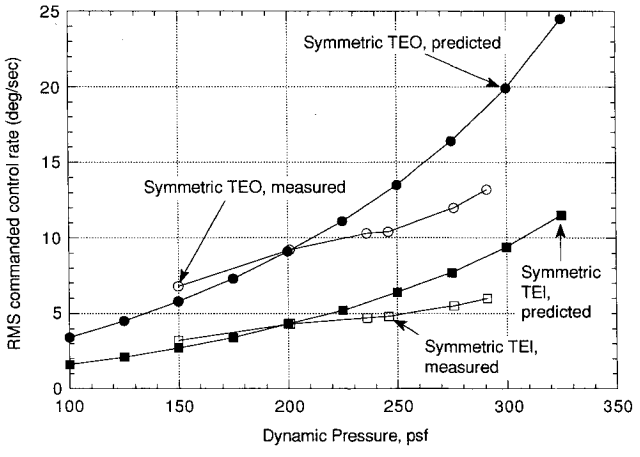

Fig. 3 Comparison of predicted vs measured control activity for a representative flutter suppression law during the 1991 tunnel entry.

that the generalized mass matrix was the identity matrix scaled by a constant.

Ground vibration tests were performed on the physical model before both tunnel entries. Mode shapes and natural frequencies corresponding to several of the lowest frequency modes were obtained and compared to the analytical predictions. Only the data corresponding to the coupled tip ballast configuration were considered to be accurate. The measured natural frequencies for these configurations were scaled to account for differences between laboratory bench mounting and wind-tunnel mounting.

In general, scaled, measured frequencies were combined with analytical mode shapes to form the aeroelastic models. For the 1989 entry, eight symmetric mode shapes and seven antisymmetric mode shapes were used. The finite element models had been tuned after the 1989 test so that analytically generated frequencies agreed more closely with the measured frequencies. For the 1991 entry, 10 symmetric and 10 antisymmetric mode shapes were used. Where measured frequencies could not be clearly matched with analytical mode shapes, analytical frequencies were used.

Aerodynamic Model

The unsteady aerodynamics induced by the elastic motion of the AFW were computed using the doublet-lattice[15] lifting surface method as implemented in the ISAC[16] system of computer codes. Doublet-lattice theory is a linear, frequency-domain theory limited to subsonic flows. The wind-tunnel model was represented aerodynamically as a half model with a plane of symmetry (or antisymmetry) at the fuselage centerline (Fig. 4). In doublet-lattice theory, lifting surfaces are modeled as zero thickness plates with aerodynamic boxes as shown on Fig. 4. The control surfaces were modeled so that box boundaries coincided with control surface edges.

In order to improve the prediction of the aerodynamic loads induced by control surface deflection, the analytical control derivatives were corrected using wind-tunnel measurements of lift and roll moment. It was assumed that the control derivatives consisted of a rigid or zero airspeed component and a dynamic pressure-dependent elastic increment. Both analytical predictions and experimental data were decomposed into these two terms; the analytical portions were then scaled to match the experimental portions.

An extensive tradeoff study was performed modeling the tip ballast stores either as flat plates or as slender bodies. It was subsequently decided to represent the wingtip ballast store as a flat plate. The flat plates had the same width as the actual tip ballast stores, but were reduced in length.

Aeroelastic Equations

The aeroelastic equations in a frequency domain format are, following Tiffany and Adams[9]:

$$\left\{-\omega^2\begin{bmatrix} M^{ff} & M^{fc} \\ M^{cf} & M^{cc}\end{bmatrix} + j\omega\begin{bmatrix} G^{ff} & 0 \\ 0 & 0\end{bmatrix} + \begin{bmatrix} K^{ff} & 0 \\ 0 & 0\end{bmatrix} + \frac{1}{2}\rho V^2\begin{bmatrix} Q^{ff}(\omega) & Q^{fc}(\omega) \\ Q^{cf}(\omega) & Q^{cc}(\omega)\end{bmatrix}\right\}\begin{Bmatrix}\boldsymbol{\eta} \\ \boldsymbol{\delta}\end{Bmatrix} = -\frac{1}{2}\rho V^2\begin{Bmatrix}\boldsymbol{Q}^{fg}(\omega) \\ \boldsymbol{Q}^{cg}(\omega)\end{Bmatrix}\left(\frac{\xi_g}{V}\right) - \begin{Bmatrix}\mathbf{0} \\ \boldsymbol{HM}_\delta\end{Bmatrix} \tag{6}$$

where $j = \sqrt{-1}$, ω is frequency in rad/s, ρ is density, V is airspeed, M, G, and K denote mass, damping and stiffness matrices, respectively, $Q(\omega)$ is a matrix of generalized aerodynamic forces, and ξ_g is an external input representing the gust mode participation coefficient.

In Eq. (6) the standard in-vacuo, second-order matrix structural equations (top row of 6) containing generalized mass, damping, and stiffness matrices are augmented with generalized aerodynamic force coefficient matrices. Equation (6) applies to either symmetric or antisymmetric motion. The elastic modes in the vector $\boldsymbol{\eta}$ are orthogonal, and so the elastic mode mass and stiffness matrices M^{ff} and K^{ff} are diagonal. Modal damping of 0.03 is assumed for each mode and is represented in the diagonal matrix G^{ff}. The elastic modes were augmented with control modes $\boldsymbol{\delta}$ that represent control surface deflection. The control modes are idealized as being control surfaces that are free to rotate, and hence have zero stiffness. Coupling between the elastic and the control modes occurs via inertial coupling M^{fc} and induced aerodynamic loads (Q^{fc} and Q^{cf}). Control mode position, rate, and accelerations are provided as inputs to Eq. (6) by the actuator transfer function [Eq. (1)]. If the control mode motion is treated as prescribed, the δ equations in (6) can be solved for the vector of hinge moments, $\boldsymbol{HM}_\delta$, which are then used in the actuator rate-limit calculations.

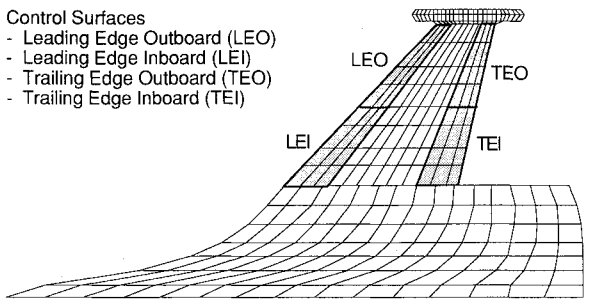

Fig. 4 Doublet-lattice aerodynamic box layout.

The matrices $Q(\omega)$ that augment the in-vacuo, second-order matrix structural equations, result from assuming steady harmonic motion when seeking a solution to the linearized form of the governing equation for unsteady, compressible flow. For subsonic flow, these solutions can be computed using the doublet-lattice theory, and the solutions are available at specific, tabulated frequencies, whose generalization would be a continuous function of frequency. To formulate the aeroelastic equations in the time-domain, it is desired to obtain the generalized aerodynamic forces as functions of the Laplace variable s. The matrix function $Q(\omega)$ can be approximated by matrix expressions that are rational in s. There are a variety of method and theories to construct rational function approximations (RFA) to the functions $Q(\omega)$, and most of them are discussed in Ref. 9. The "least square"[9,10] form of approximation is given by

$$\hat{Q}(s) = A_0 + A_1\tau s + A_2(\tau s)^2 + \sum_{m=1}^{n_{\text{lag}}} A_{2+m}\left(\frac{\tau s}{\tau s + \beta_m}\right) \tag{7}$$

where $\tau = (l/2V)$, l is a reference length, β_m is a nondimensional reduced frequency, and the A_i are matrix constants that are solved for in the approximation. The order of the least-squares-fit is indicated by n_{lag}, and is typically 1, 2, 3, or 4. The 1991 mathematical model used a four-lag approximation of the generalized aerodynamic forces. The matrix $\hat{Q}(s)$ is "hatted" to indicate that it serves as an estimate for $Q(\omega)$ when $j\omega$ is replaced by s.

The time-domain aeroelastic equations used in the simulation were derived by combining Eq. (6) (with $j\omega$ replaced by s) with Eq. (7), and are represented by the box labeled "Aeroelastic Equations" in Fig. 1. A more complete discussion of the equations used in the simulations can be found in Ref. 3.

Flutter Predictions and Frequency Response

The predicted flutter characteristics using doublet-lattice aerodynamics for a Mach number of 0.5 are shown in Table 1 along with measured characteristics. For these predictions, generalized aerodynamic force coefficients were in a frequency-domain format, and were not approximated.

Table 1 Predicted vs measured flutter characteristics

	Predicted (1991)		Measured (1991)	
	Frequency, Hz	Dynamic pressure, psf	Frequency, Hz	Dynamic pressure, psf
Symmetric	11.2	248	9.6	235
Antisymmetric, fixed in roll	10.9	233	9.1	219
Antisymmetric, free to roll	12.7	432	—	—

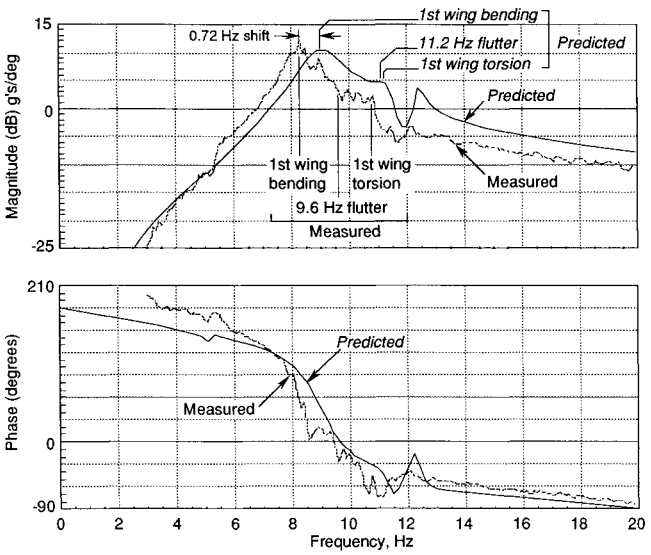

Fig. 5 Predicted vs measured (1991 test) magnitude and phase responses of the symmetric component of the tip accelerometer signal to commanded TEO control surface at 225 psf shown as functions of frequency.

Figure 5 shows a comparison of the predicted and measured frequency response of the symmetric component of the tip accelerometer signal to commanded trailing-edge outboard control surface deflection at 225 psf. Note that 225 psf is below both the analytically predicted and experimentally determined flutter dynamic pressure (see Table 1). The frequency shift between the predicted and measured peak responses is about 0.7 Hz and is seen clearly in the Bode plots of Fig. 5. Indicated on Fig. 5 are the coupled aeroelastic modes at 225 psf that are dominated by and identified with the in-vacuo vibration modes characterized as first wing-bending and first wing-torsion. The difference in frequency between measured and predicted first wing torsion modes is about the same as the first wing-bending peaks, but is obscured by the insensitivity of the tip accelerometer to the first wing torsion mode. The tip accelerometer is located near the first wing-torsion node line. Eigenvalue analysis of the analytical model was used to determine the location of the first wing-torsion mode along the frequency axis, and it is assumed the actual first wing-torsion mode is similarly situated along the measured Bode plot.

It is worth noting that the frequency of the empirically determined flutter mechanism (which occurred at about 235 psf), is roughly halfway between wing first-bending and wing-first torsion. The classical bending/torsion flutter mechanism occurs when the bending mode stiffens and the torsion mode softens as dynamic pressure is increased, allowing the modes to coalesce. The actual mechanism showed a stiffening/softening process occurring equally for both modes. The predicted flutter point (11.2 Hz at 248 psf), shows that almost no further softening of the wing first-torsion mode was occurring in the analytical model as dynamic pressure increased from 225 psf to the analytical flutter point. As a result, predicted mode coalescence occurs at both a higher frequency and a higher dynamic pressure than would be the case if the predicted first-torsion mode softened in a manner more consistent with the measured result. Since the analytical in-vacuo frequencies generally agreed with ground vibration test results, the discrepancies indicated in Table 1 and Fig. 5 must arise in the prediction of the generalized aerodynamic forces and/or the mode shapes. No satisfying explanation for the frequency shift has been determined.

Hot-Bench Time Scaling

The AFW hot-bench simulation operated at a time scale slower than 1:1 (real time). Time-scale is a function of the integration step h, and the real-time computer frame time T. If T is larger than h, the simulation runs at $1:(T/h)$ "slow." Simulating the anti-aliasing filters ensured that all dynamic elements in the hot-bench loop were digital. Therefore, the hot-bench loop could be run synchronously at a slow time-scale and dynamic validity would be maintained.

Several factors prevented the AFW hot-bench simulation from operating in real time on the LaRC central facility. The control computer ran at 200 Hz in the wind tunnel. To prevent excessive sampling-induced time delays, the hot-bench simulation updated twice for each digital controller frame. A 400-Hz (2.5-ms) hot-bench simulation update rate was therefore required for real-time operation. In preparation for the 1991 test, the mathematical model was reworked in an attempt to improve the ability to predict responses observed in the 1989 tests. As a result, the aeroelastic portion grew from 73 states in the 1989 mathematical model to 172 states in the 1991 mathematical model.[4] The compute time requirements of the full 1991 math model exceeded a 2.5-ms frame time by a factor of 10 or more.

During the hot-bench testing phase of the AFW program, many research programs competed for the two production real-time computers. Consequently, the AFW hot-bench simulation often shared a real-time computer with another job. To accommodate the reduced computing power available in that case, the simulation update rate would be further reduced. Time-scale was therefore required to be an easily adjusted parameter for any dynamic component in the hot-bench loop.

Hot-bench testing using the 1989 math model revealed that, from a productivity standpoint, a baseline time-scaling factor of 1:5 was the slowest allowable for effective testing. To run slower meant that too few data-taking runs could be performed in a 2–3-h hot-bench testing session. To achieve a 1:5 time-scaling, the 1991 aeroelastic portion of the mathematical model needed to be reduced from 172 states to about 80 states.

Reduction Method and Application

Description of the Method

The model reduction method described herein is based on transforming a stable subspace of the full dynamic model to internally balanced coordinates. The method given below builds on work described in Ref. 7. The major difference between the method presented herein and derivations found in Ref. 7 is in the calculation of the transformation matrix T, discussed

in step 6 below. More complete treatments of the properties of singular value decompositions, controllability and observability grammians, and Hankel singular values are found in Refs. 6–8. The intent of the following is to outline the steps required to implement the method and describe its virtues and limitations.

Consider the linear, time-invariant, possibly unstable dynamic system defined by

$$\begin{Bmatrix} \dot{x} \\ y \end{Bmatrix} = \begin{bmatrix} A & B \\ C & D \end{bmatrix} \begin{Bmatrix} x \\ u \end{Bmatrix} \tag{8}$$

and referred to throughout this article by the partitioned real system matrix

$$\begin{bmatrix} A & B \\ C & D \end{bmatrix}$$

Step 1

Scale the system inputs and outputs to units of similar significance. More is said about scaling in a subsequent section on application of the method.

Step 2

Transform the system of Eq. (8) into coordinates that decouple the stable and unstable portions of the model

$$\begin{Bmatrix} \dot{x}_u \\ \dot{x}_s \\ y \end{Bmatrix} = \begin{bmatrix} A_u & 0 & B_u \\ 0 & A_s & B_s \\ C_u & C_s & D \end{bmatrix} \begin{Bmatrix} x_u \\ x_s \\ u \end{Bmatrix} \tag{9}$$

where the eigenvalues of A_s are strictly stable.

Step 3

Calculate the controllability grammian X, and the observability grammian Y, of the stable subsystem by solving their associated Lyapunov equations

$$\begin{aligned} A_s X + X A_s^T + B_s B_s^T &= 0 \\ A_s^T Y + Y A_s + C_s^T C_s &= 0 \end{aligned} \tag{10}$$

Step 4

Perform a singular value decomposition on the controllability grammian

$$U_x \Sigma_x V_x^T = X \tag{11}$$

where Σ_x is a diagonal matrix of positive real numbers, and U_x and V_x are real, square orthonormal ($U_x U_x^T = V_x V_x^T = I$) matrices. Since X is both symmetric and positive semidefinite, $U_x = V_x$ and the decomposition in Eq. (11) can be written as

$$U_x \Sigma_x U_x^T = X \tag{12}$$

Since Σ_x is diagonal, $\Sigma_x^{1/2}$ will refer to a diagonal matrix whose diagonal elements are the square roots of the diagonal elements of Σ_x.

Step 5

Perform a second singular value decomposition on the real symmetric, positive semidefinite product

$$U_x \Sigma_x^{1/2} U_x^T Y U_x \Sigma_x^{1/2} U_x^T \tag{13}$$

to give

$$U_w \Sigma_w U_w^T = U_x \Sigma_x^{1/2} U_x^T Y U_x \Sigma_x^{1/2} U_x^T \tag{14}$$

where Σ_w is a diagonal matrix of nonnegative real numbers ordered in decreasing magnitude.

Step 6

A transformation matrix T is then formed

$$T = U_x \Sigma_x^{1/2} U_x^T U_w \tag{15}$$

If n_s is the order of the square matrix A_s, and n_{sr} is the order of the desired reduced-order model, then the following partitioning of T, and its inverse T^{-1}, can be defined,

$$[T_1 \quad T_2] = T \quad \text{and} \quad \begin{bmatrix} U_1^T \\ U_2^T \end{bmatrix} = T^{-1} \tag{16}$$

where T_1 is $n_s \times n_{sr}$, and U_1 is $n_s \times n_{sr}$.

It should be noted that the transformation T is equivalent to the transformation formed in Ref. 7. If Eq. (14) is multiplied on the left by $(U_x \Sigma_x^{1/2} U_x^T)$, and on the right by $(U_x \Sigma_x^{-1/2} U_x^T)$, the following result is obtained:

$$T \Sigma_w T^{-1} = XY \tag{17}$$

Thus, T that is achieved in Eq. (15), by singular value decompositions, is the same T that is achieved by an eigenvalue decomposition of the product XY, as shown in Eq. (17), and as discussed in Ref. 7.

It should also be noted that unless $(A_s \quad B_s)$ is a completely controllable pair, the diagonal matrix $\Sigma_x^{1/2}$ will contain one or more zeros on the diagonal, rendering T singular. If T is singular, T^{-1} will not exist, and T will not be a transformation matrix. Steps 4–6 therefore require that $(A_s \quad B_s)$ be a completely controllable pair, or equivalently, X be positive definite ($X > 0$), not merely positive semidefinite.

Step 7

Partition the stable subsystem. When the stable subsystem is transformed according to the matrix T, the new, internally balanced states are ordered according to their contribution to peak frequency response magnitude over all output/input pairs. This ordering is discussed in a subsequent section on error properties. A reduced-order model of the stable subsystem can now be formed by the following equations:

$$\begin{bmatrix} A_{sr} & B_{sr} \\ C_{sr} & D_{sr} \end{bmatrix} = \begin{bmatrix} U_1^T A_s T_1 & U_1^T B_s \\ C_s T_1 & D \end{bmatrix} \tag{18}$$

Step 8

Recombine the reduced stable subsystem with the unstable subsystem. The matrix A_{sr} will generally be fully populated. Transform the reduced-order stable subsystem

$$\begin{bmatrix} A_{sr} & B_{sr} \\ C_{sr} & D_{sr} \end{bmatrix}$$

to a real Jordan form to minimize computations required for implementing the discretized form of the reduced system. The real Jordan form is diagonal up to 2×2 blocks for independent eigenvectors. The near diagonal reduced-order stable subsystem can then be recombined with the unstable subsystem of the original dynamic system to form a reduced-order form of the original, possibly unstable, dynamic system

$$\begin{bmatrix} A_r & B_r \\ C_r & D_r \end{bmatrix} = \begin{bmatrix} A_u & 0 & B_u \\ 0 & A_{sr} & B_{sr} \\ C_u & C_{sr} & D \end{bmatrix} \tag{19}$$

Step 9

Scale the reduced system back to original units.

Numerical Robustness of the Method

Prior to implementing the procedures described above, a method was first attempted wherein a commercial package

was invoked to provide the internally balanced representation of a stable system achieved by T, in step 6. It is not known what method the commercial package used to achieve an internally balanced representation, but the command consistently failed and reported a problem with performing a Choleski decomposition. It should be noted that this same commercial package worked fine for smaller systems. The authors believe that the use of singular value decompositions, well-known for their numerical stability, to calculate T make the approach outlined in steps 1–9 attractive.

Error Properties of the Method

Having formed a reduced-order model, it is important to know how well it approximates the full-order model. Define a frequency response error matrix E_{sr} by differencing the full and reduced stable systems

$$E_{sr}(j\omega) = C_s(j\omega I - A_s)^{-1}B_s - C_{sr}(j\omega I - A_{sr})^{-1}B_{sr} \quad (20)$$

Let the n_s diagonal elements of $\Sigma_w^{1/2}$ defined in Eq. (14) be denoted by $\sigma_h(i)$ (the Hankel singular values[6]). A magnitude bound[6,7] on the error matrix E_{sr} is given by

$$\sup\{\bar{\sigma}[E_{sr}(j\omega)],\ \forall\omega\} \leq \varepsilon_B = 2\sum_{i=n_{sr}+1}^{n_s}\sigma_h(i) \quad (21)$$

so that the maximum singular value of the error matrix over all frequencies is less than or equal to twice the sum of the Hankel singular values associated with the removed $n_s - n_{sr}$ states. The maximum singular value of a matrix can be interpreted as

$$\bar{\sigma}[E_{sr}] = \sup\{E_{sr}u,\ \|u\| = 1\} \quad (22)$$

Thus, the maximum magnitude response of E_{sr} in any direction for a harmonic input of unit size is bounded by ε_B. In particular, the magnitude of the largest element of $E_{sr}(j\omega)$ is bounded by ε_B. The significance of this well-known result for internally balanced realizations cannot be overstated. Once the labor of steps 1–5 are performed, the quality of the reduced-order model to be generated for any selection of n_{sr} can be determined prior to performing steps 6–9. Furthermore, since the stable and unstable portions have been decoupled [Eq. (9)], the result of Eq. (21) holds for the error matrix associated with the complete system

$$E_r(j\omega) = C(j\omega I - A)^{-1}B - C_r(j\omega\mathrm{I} - A_r)^{-1}B_r \quad (23)$$

Application of the Method

In the 1991 mathematical model, the 172 state aeroservoelastic model (see Fig. 1) constituted the bulk of the required computations in the equations of motion. When the aeroservoelastic model was written in matrix form as in Eq. (8), the A, B, and C matrices are highly populated. Even if the system were transformed to coordinates where A was diagonal, full matrix multiplications would still be required for B (172 × 10) and C (56 × 172). On the other hand, the computational load of implementing a discretized form of Eq. (8) for the anti-aliasing filter portion of the dynamic model was small when compared to the aeroelastic portion. The 40 anti-aliasing filter equations were uncoupled. When written in matrix form, the A, B, and C matrices were square and diagonal, and the matrix D was zero. The aeroelastic model was therefore chosen for application of the model reduction method.

Maintaining the 1:5 time-scaling required that the aeroelastic model, with 172 states, 10 inputs and 56 outputs, be reduced to a system with approximately 80 states that would accurately replicate the full-order input-output results for all 560 combinations. As described in Ref. 3 and depicted in Fig. 1, the hot-bench simulation is derived by extracting linear aeroelastic models from the batch simulation that are valid for a particular dynamic pressure. To provide sufficient continuity for hot-bench testing, linear aeroelastic submodels were extracted and reduced for nine different dynamic pressures, ranging from 150 to 350 psf, in increments of 25 psf. This process was repeated for two wind-tunnel model test configurations (and by extension, for the batch simulation). The two configurations were 1) the model fixed in roll and 2) the model free to roll.

A requirement of any reduction process is the scaling of the inputs and outputs to units of similar significance. The first 8 inputs (actuator commands), and the first 40 outputs (sensors), of the simulation correspond to analog lines on the wind-tunnel model. For these inputs and outputs, a natural selection for units was volts. The two turbulence inputs were scaled so that an intensity of one standard deviation was weighted the same as 1 V. The 16 outputs representing elastic mode deflection were left unchanged.

The analog to digital (A/D) converters in the digital controller yield 12 bits of resolution for inputs with a range of ±10 V. If an error bound of $\varepsilon_B = 20/2^{12}$ had been satisfied, then for a harmonic signal into any input, the difference between the full mathematical model and the reduced model at any output would have been less than the resolution of the A/D converters. For the scaling described above, error bounds tighter than $20/2^{10}$ produced models too large for the hot-bench timing budget. Since the error bound represents a worst-case error, and differences in the last two bits of a converted signal would be small compared to electrical noise in the wind tunnel and inaccuracies in the mathematical model, an error bound of $\varepsilon_B = 20/2^{10}$ was used. This choice for an error bound was validated by time-history comparisons between the batch and the resulting hot-bench simulation. Once an error bound is determined, the order of the candidate reduced model n_{sr} was varied until the required accuracy was achieved according to the definition of Eq. (22). This ensured that the reduced-order aeroelastic model would retain 10 of the 12 bits of precision available through the A/D converters. For each of the reduced-order models formed at 9 dynamic pressures, no more than 82 states were required. The 82-state model was required at the highest dynamic pressure of 350 psf, where the unstable portion was larger than for the lower dynamic pressures due to the formation of a second flutter mode.

Step 2 was implemented by transforming the system of Eq. (8) to real Jordan form. For the dynamic systems considered in this study, the eigenvectors were independent, resulting in real Jordan forms wherein all nonzero elements of the transformed A matrix are either real 1×1 ($[\sigma]$) or real 2×2 $[\sigma \quad -\omega/\omega \quad \sigma]$ blocks on the diagonal. The 2×2 blocks correspond to system eigenvalues that were complex conjugate pairs, with σ being the real part, and ω being the imaginary part. Corresponding rows and columns of the resulting system matrix could then be permuted, taking care to preserve the integrity of the complex conjugate pairs, until all the blocks corresponding to unstable eigenvalues ($\sigma \geq 0$) were in the upper left corner of the system matrix. The result was a system of the form where the eigenvalues of A_s are strictly stable ($\sigma < 0$).

Results of Math Model Reduction

Frequency and time-response comparisons between full-order (172 states) and reduced-order linear aeroelastic models for selected input-output combinations are shown in Figs. 6–9. These responses (Figs. 6–9) are for input-output pairs corresponding to the $u_{\text{lin}} - y_{\text{lin}}$ locations in Fig. 1, and are for the case of the simulated wind-tunnel model being free to roll and at a dynamic pressure of 300 psf. This dynamic pressure is well past predicted instability and ensures that the portion of the reduction method that preserves the unstable dynamics is demonstrated.

Figure 6 shows comparisons of full and reduced models for the case of the transfer function consisting of the right wingtip

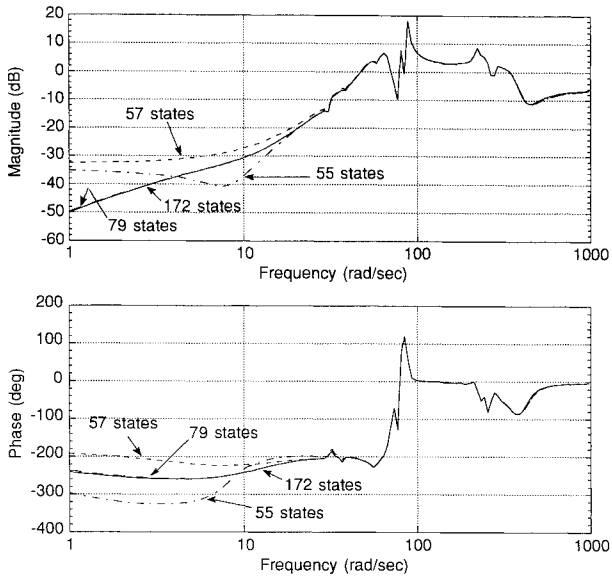

Fig. 6 Frequency response of the right tip accelerometer to commanded right TEO control for various levels of model reduction at a dynamic pressure of 300 psf, free-to-roll.

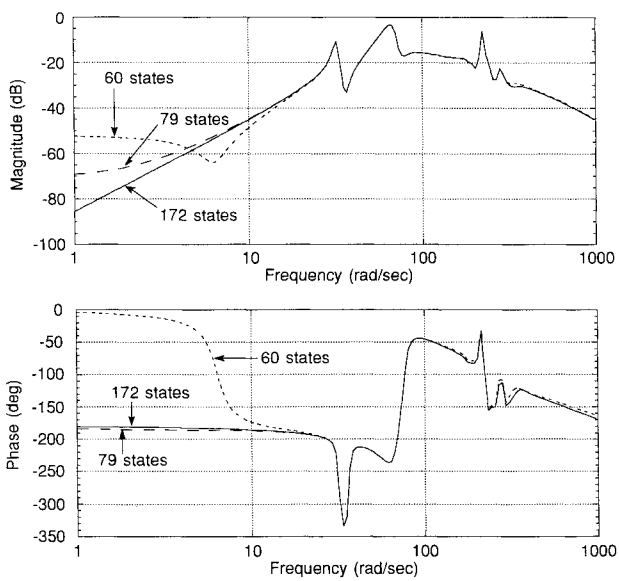

Fig. 7 Frequency response of the right tip accelerometer to symmetric turbulence input for various levels of model reduction at a dynamic pressure of 300 psf, free-to-roll.

accelerometer response to the right trailing-edge actuator command. The response of the 79-state ($\varepsilon_B = 20/2^{10}$) model is indistinguishable from the full model response for the frequency range shown. Responses for 57-state ($\varepsilon_B = 20/2^3$) and 55-state ($\varepsilon_B = 20/2^2$) models are also shown. For the input-output pair shown in Fig. 6, the reduction process must be applied fairly aggressively before the reduced-model response departs from the full-order model. The property of an IB-based reduction method to match peak frequency response is clearly demonstrated.

Figure 7 shows the response of same right tip accelerometer to a symmetric turbulence input. In this case the 79-state model does depart somewhat from the full model, and one need only go to the 60-state ($\varepsilon_B = 20/2^5$) model to produce substantial departure. The response shown in Fig. 6 appears to be fitted better by the 79-state model because the peak response shown in Fig. 6 is 20 dB higher than the peak response shown in Fig. 7. Note that the 79-state model is exact down to -40 db for both figures.

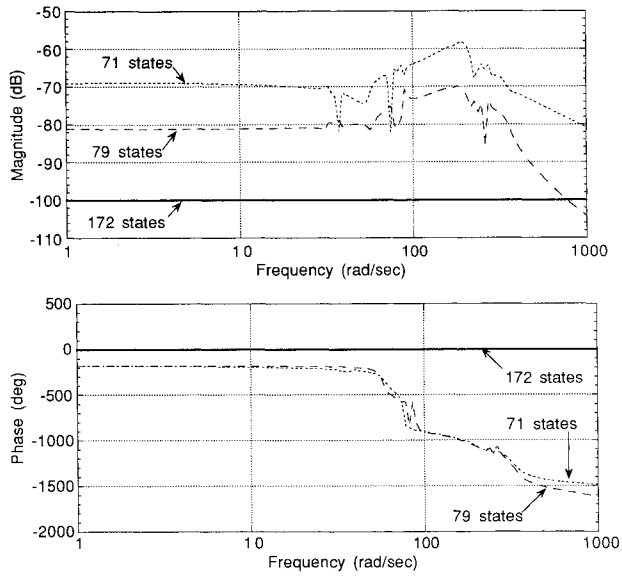

Fig. 8 Predicted frequency response of the left LEO control surface to a command at the right TEO actuator for various levels of model reduction at a dynamic pressure of 300 psf, free-to-roll.

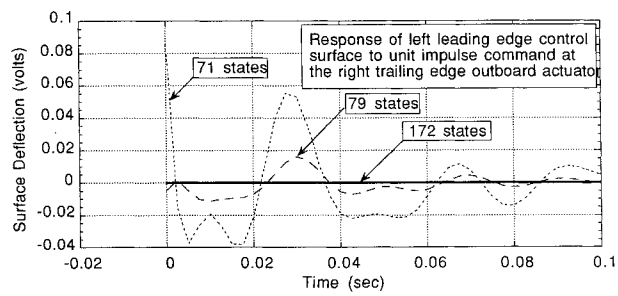

Fig. 9 Predicted time response of the left LEO control surface to a command at the right TEO actuator for various levels of model reduction at a dynamic pressure of 300 psf, free-to-roll.

Figures 8 and 9 show the predicted frequency and time responses of the left leading-edge outboard (LEO) control surface position due to a command at the right trailing-edge outboard (TEO) actuator for various levels of model reduction at a dynamic pressure of 300 psf in the free-to-roll condition. The response of the full-order, 172-state, linear aeroservoelastic model (shown by the heavy solid line) is zero. This is seen clearly in the time response of Fig. 9. The plotting software used to create Fig. 8 arbitrarily plots a zero frequency response as -100 dB magnitude and 0-deg phase. Note that responses that are identically zero in the full model are allowed to become nonzero in the reduced models.

Also of interest is the end-to-end time response comparison between the complete batch simulation and the complete hot-bench simulation model. The end-to-end comparison includes the effects of the anti-aliasing filter dynamics and nonlinear actuator dynamics that were not reduced. Responses of both batch and hot-bench simulations were calculated for a 1-V (2.67-deg) step command to the right TEO actuator for the free-to-roll condition at a dynamic pressure of 225 psf. The time response agreement was uniformly excellent for all outputs. The right and left tip accelerometer responses, which are typical cases, are shown in Fig. 10. These input-output pairs corresponding to the $u_{nl} - y_{nl}$ locations in Fig. 1. In each case, batch ("full math model") and hot-bench simulation responses are plotted vs the left vertical axis and cannot be distinguished. The difference between the batch and hot-bench result is plotted vs the right vertical axis. The scaling on the right axis is 1/100 of the left axis. In each case, the differences are of the order of millivolts and tend to peak where the batch response is changing rapidly.

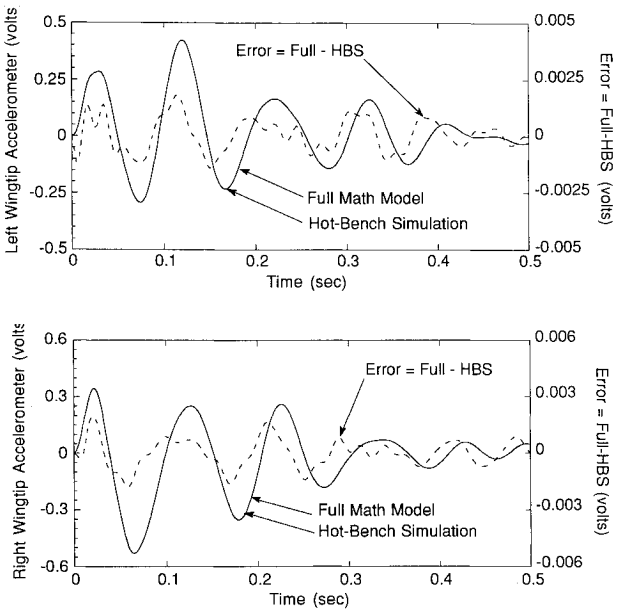

Fig. 10 Comparison between a full order batch simulation and the hot-bench simulation with a 79-state aeroelastic model for the right and left tip accelerometers for a 1-V step command to the right TEO control surface at a dynamic pressure of 225 psf, free-to-roll.

More advanced model reduction techniques employ frequency weighting filters to discount selected frequency regions of the full model.[7,8] In a frequency-weighted approach, weighting filters would be applied to either all the input signals or all the output signals. While lower-order final models can be achieved by bounding the frequency range of interest, the application of frequency weighting raises three concerns. Foremost is the absence of a guaranteed bound of the form of Eq. (21). The presence of such a bound for the IB method obviates the need for extensive checking of all possible input-output combinations in the reduced models. However, work on the formulation of such a bound has been reported in Ref. 17. A second concern is that adding weighting filters imposes a computational and numerical robustness burden by effectively raising the order of the full plant to be reduced. Solving the Lyapunov equation [Eq. (10)] for a symmetric controllability grammian X of dimension 100×100 is analogous to solving a linear system of equations for $5050 = [(101)(100)/2]$ unknowns. Raising the order of X by 10 raises the order of the associated Lyapunov solution from 5050 to 6105. The third issue concerns time responses. Since the internally balanced approach ensures a good match in peak frequency response over the entire frequency range, equivalent responses in both the frequency and time domains between the full- and reduced-order models are ensured for arbitrary input. If a reduced-order plant is produced by de-emphasizing selected frequency components, a step input, which has broadband frequency content, would produce a different time response from the full-order model. Band limited inputs would be required to produce matching time histories. This property should not be a concern as long as it is anticipated and understood.

The classical IB approach in combination with the numerically robust method of calculation presented herein and the system scaling chosen, was well-suited to the problem of reducing an aeroelastic simulation model. A procedure was constructed that worked for all 18 (9 dynamic pressure $\times$ 2 boundary conditions) cases without intervention. The simulation model had to give results indistinguishable from the batch simulation to support validation testing of the digital controller. The large number of states, inputs, and outputs would have made the application of frequency-weighted methods difficult and, for the target model size required, unnecessary.

Concluding Remarks

Modern model reduction techniques were successfully applied to a time-scaled hot-bench simulation of an aeroelastic system. The model reduction method is based on transforming a stable subsystem to internally balanced coordinates. The internally balanced approach was particularly effective at removing the aerodynamic lag states that are often part of linear aeroelastic systems.

Since the internally balanced approach ensures a good match over the entire frequency range, equivalent responses in both the frequency and time domains between the full-order and reduced-order models are ensured. The equivalent time and frequency responses significantly simplified the hot-bench validation process.

Finally, the error bound properties of the internally balanced decomposition greatly enhance its usefulness in model reduction. The need for extensive checking of all possible input-output combinations in the reduced models is obviated. However, numerical conditioning can be an issue when trying to perform internally balanced decompositions of large aeroelastic systems, and caution is recommended.

References

[1]Miller, G. D., "Active Flexible Wing (AFW) Technology," Air Force Wright Aeronautical Labs., AFWAL-TR-87-3096, Feb. 1988.

[2]Perry, B., III, Cole, S. R., and Miller, G. D., "A Summary of the Active Flexible Wing Program," AIAA Paper 92-2080, April 1992.

[3]Buttrill, C. S., and Houck, J. A., "Hot-Bench Simulation of the Active Flexible Wing Wind-Tunnel Model," AIAA Paper 90-3121, Sept. 1990.

[4]Buttrill, C. S., and Bacon, B. J., "Model Order Reduction Applied to a Hot-Bench Simulation of an Aeroelastic Wind-Tunnel Model," AIAA Paper 91-2935, Aug. 1991.

[5]Moore, B., "Principal Component Analysis in Linear Systems: Controllability, Observability, and Model Reduction," *IEEE Transactions on Automatic Control*, Vol. AC-26, No. 1, 1981, pp. 17–32.

[6]Glover, K., "All Optimal Hankel-Norm Approximations of Linear Multivariable Systems and their L^∞-Error Bounds," *International Journal of Control*, Vol. 39, No. 6, 1984, pp. 1115–1193.

[7]Enns, D., "Model Reduction for Control System Design," Ph.D. Dissertation, Dept. of Aeronautics and Astronautics, Stanford Univ., Stanford, CA, June 1984.

[8]Bacon, B. J., "Order Reduction for Closed-Loop Systems," Ph.D. Dissertation, School of Aeronautics and Astronautics, Purdue Univ., West Lafayette, IN, Dec. 1991.

[9]Tiffany, S., and Adams, W., "Nonlinear Programming Extensions to Rational Function Approximation Methods for Unsteady Aerodynamic Forces Which Allow Variable Selection of Constraints," NASA TP-2776, May 1988.

[10]Tiffany, S., and Karpel, M., "Aeroservoelastic Modeling and Applications Using Minimum-State Approximations of the Unsteady Aerodynamics," AIAA Paper 89-1188, April 1989.

[11]Hoblit, F., *Gust Loads on Aircraft: Concepts and Applications*, AIAA Education Series, AIAA, Washington, DC, 1988, p. 45.

[12]Adams, W., Christhilf, D., Waszak, M., Mukhopadhyay, V., and Srinathkumar, S., "Design, Test, and Evaluation of Three Active Flutter Suppression Controllers," NASA TM-4338, Oct. 1992.

[13]Perry, B., III, et al., "Digital-Flutter-Suppression-System Investigations for the Active Flexible Wing Wind-Tunnel Model," AIAA Paper 90-1074, April 1990.

[14]Christhilf, D. M., and Adams, W. M., Jr., "Multifunction Tests of a Frequency Domain Based Flutter Suppression System," AIAA Paper 92-2096, April 1992.

[15]Giesing, J., Kalman, T., and Rodden, W., "Subsonic Unsteady Aerodynamics for General Configurations. Part I, Vol. I—Direct Application of the Nonplanar Doublet-Lattice Method," Air Force Flight Dynamics Lab., AFFDL-TR-71-5, Pt. I, U.S. Air Force, Nov. 1971.

[16]Peele, E., and Adams, W. M., Jr., "A Digital Program for Calculating the Interaction Between Flexible Structures, Unsteady Aerodynamics, and Active Controls," NASA TM-80040, Jan. 1979.

[17]Newman, B., and Schmidt, D., "New Plant and Controller Order Reduction Results with Weighted Balancing," AIAA Paper 91-2805, Aug. 1991.